2024

IMPROVING CAST STEEL RAIL COUPLER FATIGUE RESISTANCE THROUGH LOCAL WIRE-ARC ADDITIVE MANUFACTURING

Andrew M. Bunge
Michigan Technological University, ambunge@mtu.edu

IMPROVING CAST STEEL RAIL COUPLER FATIGUE RESISTANCE THROUGH LOCAL WIRE-ARC ADDITIVE MANUFACTURING

By

Andrew M. Bunge

A THESIS

Submitted in partial fulfillment of the requirements for the degree of

MASTER OF SCIENCE

In Materials Science and Engineering

MICHIGAN TECHNOLOGICAL UNIVERSITY

2024

This thesis has been approved in partial fulfillment of the requirements for the Degree of MASTER OF SCIENCE in Materials Science and Engineering.

Department of Materials Science and Engineering

Thesis Advisor: *Paul G. Sanders*

Committee Member: *Vinh T. Nguyen*

Committee Member: *Douglas J. Swenson*

Department Chair: *Walter W. Milligan*

Contents

Author Contribution Statement

Acknowledgement should be given to Sam Vellequette, a fellow student at Michigan Technological University. Although he was not involved in the writing process, he was a valuable asset in conducting experiments and producing samples. He will be continuing the work on this project.

Abstract

Every year, thousands of cast-steel railcar couplers suffer from corrosion-initiated fatigue cracking in similar areas of the coupler's knuckle; between 2015 and 2018 about 90,000 knuckles were replaced, otherwise these couplers would have been at risk for unexpected failures. These types of couplers have been common in industrial use as early as 1932, hence it is desirable for a countermeasure to the fatigue cracking that does not involve significantly altering the geometry or casting process. Wire arc additive manufacturing (WAM) is a developing technology which boasts the ability to produce complex near-net-shape components; however, less attention has been paid to WAM's potential for local enhancements to typical failure zones. By replacing the cast steel in the region of the knuckle that contains these high-stress failure points with fatigue and corrosion resistant WAM deposits, the whole knuckle receives a longer service life while maintaining its mechanical properties and overall geometry. The efficacy of this procedure comes down to the ability to print WAM deposits with less defects than the base steel while introducing alloying elements (nickel, chromium, molybdenum) to prevent corrosion; this is accomplished by utilizing gas tungsten arc welding (GTAW) in the WAM process with commercially available low-alloy filler wire prior to optimization using the knuckle's heat treat schedule then validated by fatigue testing the resulting components. Selective use of WAM technology to aid in the high-volume production of parts through local enhancements could be a step to efficiently utilize its capabilities in industry.

Introduction

The rail industry transports thousands of tons of goods by linking multiple railcars together utilizing a coupler on each end, allowing modular car arrangement. The most common coupler mechanism used in the United States is the Association of American Railroads (AAR) E-type coupler, which utilizes a "knuckle" that is able to pivot into contact with a mating knuckle (Figure 1). Once in place, these knuckles transfer load through the mating surface to a pulling lug in the rear, which latches to the rest of the coupler assembly.

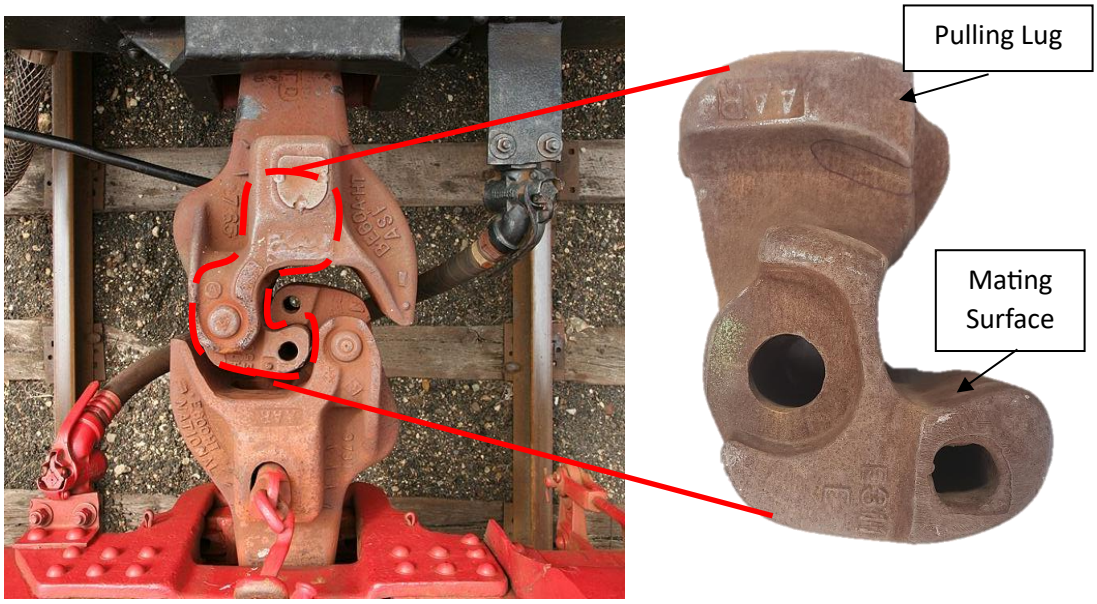

Figure 1: Two mating rail-car couplers [1] with the knuckles (outlined) mostly contained within the coupler (left). Full view of the knuckle (right).

These knuckles play a vital role in transferring load to the engine and must be inspected regularly to prevent dangerous failures (Figure 2). During these inspections, a

common failure mode is a fatigue crack that initiates in the corner of the pulling lug (Figure 3).

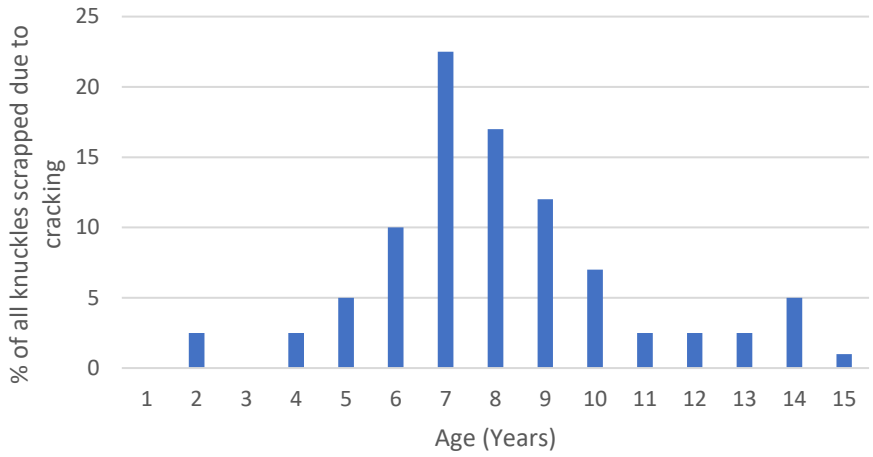

Figure 2: Histogram of failures due to pulling lug cracking [2].

Figure 3: Intact knuckle (left) and knuckle exhibiting fatigue crack in the pulling lug (right) [2]

Over 75% of knuckles are scrapped before 6 years of service, with pulling lug fatigue cracks accounting for nearly 25% of this scrap. A key detail about these failures is they occur during typical loading scenarios where a fatigue crack otherwise would not be expected. In an over-capacity loading condition, these knuckles act as the weak link, breaking to prevent damage to other more expensive components within the railcar. This coupler assembly has a long legacy, as it has been in widespread use in the United States since 1932 [3]. Being able to address this failure mode without changing the coupler geometry or strength would be highly advantageous.

The AAR E-type coupler is made from a cast steel grade used by the rail industry, appropriately referred to as Grade-E steel. It is a plain carbon steel with approximately 0.3 wt% carbon, with the only other alloying elements being 1.5 wt% silicon and 1.85 wt% manganese (Table 1).

Table 1: Grade-E chemical composition (wt%) [2]

Material	C	Si	Mn	Ni	Cr	Mo	P	S
Grade E max	0.32	1.5	1.85	N/A	N/A	N/A	0.04	0.04
Target	0.25	0.42	1.3	N/A	N/A	N/A	<0.02	<0.02
Grade E min	0.2	0.25	0.9	N/A	0.2	0	0	0

After the knuckles are cast, they are heat treated to achieve the specified strength and toughness. This quench and temper heat treatment first heats the steel to its austenitization temperature, quenches, and then tempers at a lower temperature (Table 2). The final steel property targets are 280 Brinell hardness (BHN) and 120 ksi tensile strength [4].

Table 2: Heat treat schedule of Grade-E steel knuckles (T. Petrunich, personal communication, June 14, 2020)

BATCH HEAT TREAT FURNACE CYCLE

HT PROCESS	METAL TYPE	FURNACE	ZONE SET POINTS	HT CYCLE TIME
Austenitize	**Grade E**	**Small Parts Batch**	1700°F min **Set @ 1750°F** 1800°F max	**2 hours at temp** (4 hour total)
HT PROCESS	**CASTING TEMP**	**DELAY TIME**	**QUENCH WATER TEMP**	**QUENCH CYCLE TIME**
Quench	**1650°F min** (1800°F max)	***1 minute (target)*** *2 minute (max)*	**100°F – 120°F** (155°F max)	**3 minutes** (3 ½ min max) (Based on 2 racks)
HT PROCESS	**DELAY TIME**	**FURNACE**	**ZONE SET POINTS**	**HT CYCLE TIME**
Temper (241-311 BHN)	**8 hours max**	**Small Parts Batch**	1050°F min **Set @ 1100°F** 1150°F max	**2 hours at temp** (4.5 hours total)

This Grade-E material was analyzed to determine what factors led to the development of fatigue cracks under typical loading scenarios. Three contributing factors were identified: casting defects, decarburization, and corrosion [2]. Casting defects such as porosity occur during manufacturing and are often small and undetected; decarburization occurs primarily during the austenization as part of the quench and temper heat treatment, and corrosion is caused by environmental factors during service. These three effects compound on each other in this respective order, surface cracks and pores that form during casting provide deeper penetration of decarburization effects as deeper areas of the casting are exposed to air. The situation only worsens when in service and exposed to corrosive factors.

The steel foundry industry typically repairs small defects observed in castings. If a cast piece has visible surface defects, often in the form of surface porosity, the void can be filled in with weld filler material [5]. Generally, situations that require weld

repair occur inconsistently and require a trained welder to perform the procedure. However, if a defect always occurred in the same place or if a recess or pocket was intentionally formed on the surface of a casting, an automated robotic process could be used to perform a weld repair.

Wire-arc additive manufacturing (WAM) is an alternative to subtractive manufacturing methods. WAM uses arc welding and filler wire to deposit weld material through a computer-generated path in order to build up a structure layer by layer. Intentionally forming a recess or pocket in the portion of the knuckle casting that is prone to cracking would allow for that area to be rebuilt by a local application of WAM. Utilizing this technique would decouple material selection in that region to address the three factors that contribute to accelerated fatigue cracking while maintaining the knuckle's overall geometry, strength, and manufacturing process.

Disregarding the effects of decarburization and corrosion initially, it is desired that the WAM material performs better than the baseline Grade-E in a high-cycle fatigue situation while maintaining the baseline tensile strength. This increase in fatigue resistance is attributed to the improved microstructure and toughness of the filler material. Two elements that can improve fatigue resistance are manganese (Mn) and nickel (Ni). Ni and Mn have a tendency to increase the amount of retained austenite in a microstructure [6]. Retained austenite is metastable at room temperature due to the local strain state. When a crack enters a retained austenite grain, the grain rapidly transforms into martensite, hindering crack propagation. This slowing of crack

propagation increases fatigue life [7]. When coupled with a welding process, Ni and Mn segregate to the outside of the beads due to directional solidification. These concentrations increase the retained austenite and hardness on the surface [6]. Additionally, the fatigue performance of low carbon WAM structures with small alloying additions increases with quench and temper heat treatments similar to that used in the AAR E schedule [8]. Performing the heat treatment after the WAM is deposited will also help mitigate adverse effects of the heat-affected-zone (HAZ) in the substrate material at the base of the weld.

It can be hypothesized if steel filler wire is utilized in a well-controlled WAM process then the material produced will be more fatigue-resistant than a plain carbon cast steel with similar properties because porosity and decarburization are reduced in the WAM material.

Methods

A standard method for measuring high-cycle fatigue performance is rotary bend fatigue (RBF). Samples for this test are cylindrical with a slight taper in the center to concentrate the stress (Figure 20). These samples are loaded into the RBF machine individually, and the machine applies a user-specified load downward on one end of the sample, putting the top in tension and the bottom in compression. Given the sample geometry, stress concentrates at the center of the hourglass shape, and as the sample is rotated, these stress concentrations travel around the circumference of the cross-section, producing a fully reversed loading cycle. This rotation is performed at 60 Hz,

allowing for 10,000,000 cycles to be performed in 2 days. This technique allowed for relatively fast high-cycle fatigue testing of WAM printed and Grade-E cast samples.

WAM Printer Setup

To produce the WAM samples, the decision was made to build a WAM printer at Michigan Technological University. The main components necessary for a WAM printer are a method of tool head movement, a power source for welding, integration of components, and process control capabilities.

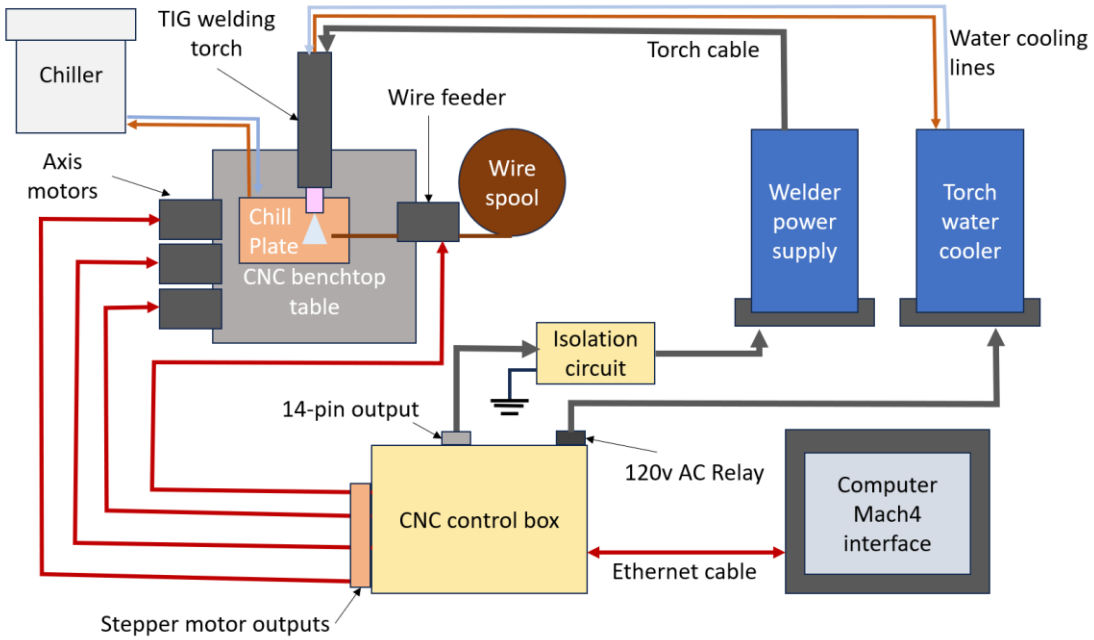

Figure 4: Michigan Tech WAM system overview.

There is a wide variety of strategies for moving a toolhead in three-dimensional space. Multi-joint robotic arms offer a large range of motion and many degrees of freedom but are large and expensive with complex programming. The advantages of this type of system are lost with small build volumes. Instead, a four-axis benchtop

CNC table was selected for the printer for easier programming and modification. The table consists of a gantry over the work area with motion controlled on the X, Y, and Z axes through the use of multiple stepper motors, with the fourth axis used to drive the weld-wire feeder. The total range of motion is a 24” x 24” x 8” rectangular volume, acceptable for producing small rotary-bend fatigue samples. The CNC table (Benchtop PRO 2424 2' x 2' CNC Machine) and control box (Plug and Play NEMA 23 CNC Control System, CRP800-00E-5) were purchased from AVID CNC, along with the Mach4 control software (Warp9Mach4, version no. 1.0.1.277.1). This product communicates with a desktop computer through an ethernet cord.

Most commercially available weld wire feeders rely on DC motors. To integrate a wire feeder with the CNC control box, it was necessary to replace this DC motor with a high-torque stepper motor matching the other drive axes. The control box has support for a 4^{th} axis to actuate this wire-feed stepper motor. To enable this substitution, a custom filament 3-D printed gearbox enclosure was made to replace the back of the wire feeder’s original gearbox, and a spider coupling was welded to one of the gears to ease meshing with the drive motor (Figure 5, Figure 6).

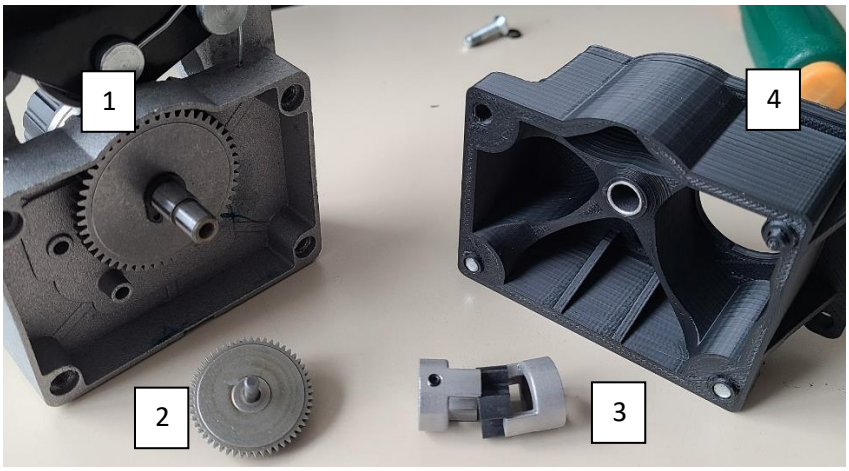

Figure 5: Disassembled wire-feed gearbox. 1: The main wire feeding body responsible for pinching and advancing the wire, 2: An original gear to which the spider bushing is welded, 3: Spider bushings that account for any misalignment between the gear and the shaft, 4: 3D-printed housing which the stepper motor attaches to.

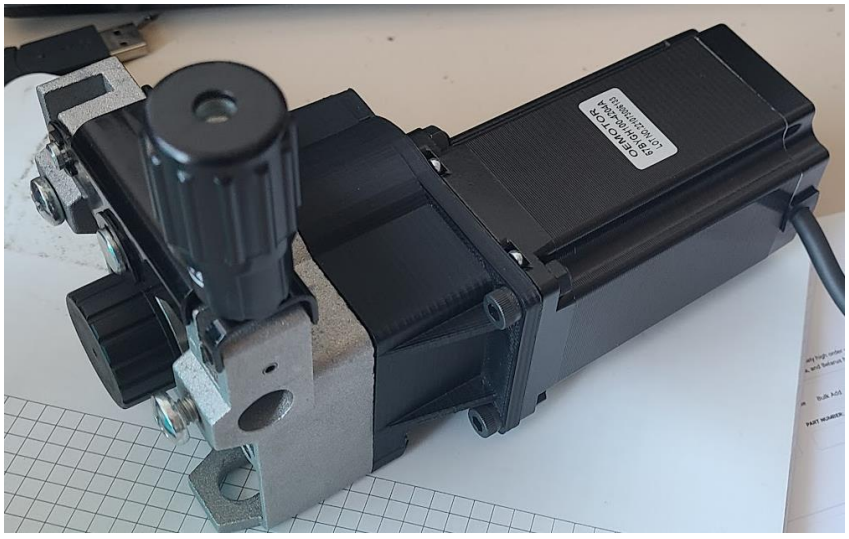

Figure 6: Complete wire feed mechanism assembly.

The welding power supply needed to fulfill certain criteria, including an adequate duty cycle for the given power range. Depending on the welding power supply and power needed for the workpiece, an ON/OFF “duty” cycle is selected to prevent power supply overheating or component failure. Ideally, a welding power supply could provide a 100% ON duty cycle for continuous WAM printing at the

desired power level. Another necessity is a welding power supply unit with TIG (tungsten inert gas) capability. A TIG welding process was chosen over a MIG (metal inert gas) process (Figure 7). With MIG welding, the filler wire acts as the electrode that forms the plasma arc, which couples heat input and material input, limiting control over the process. In TIG welding, a tungsten rod acts as the electrode, separating the heat input from the filler wire feed. The high melting point of tungsten and convective cooling by the cover gas prevents the electrode from melting or deforming. The stability of the electrode means that a plasma arc can be initiated at the start of the welding process and maintained until the end. During this, a melt "pool" is formed by the arc on the substrate to which filler material can be added.

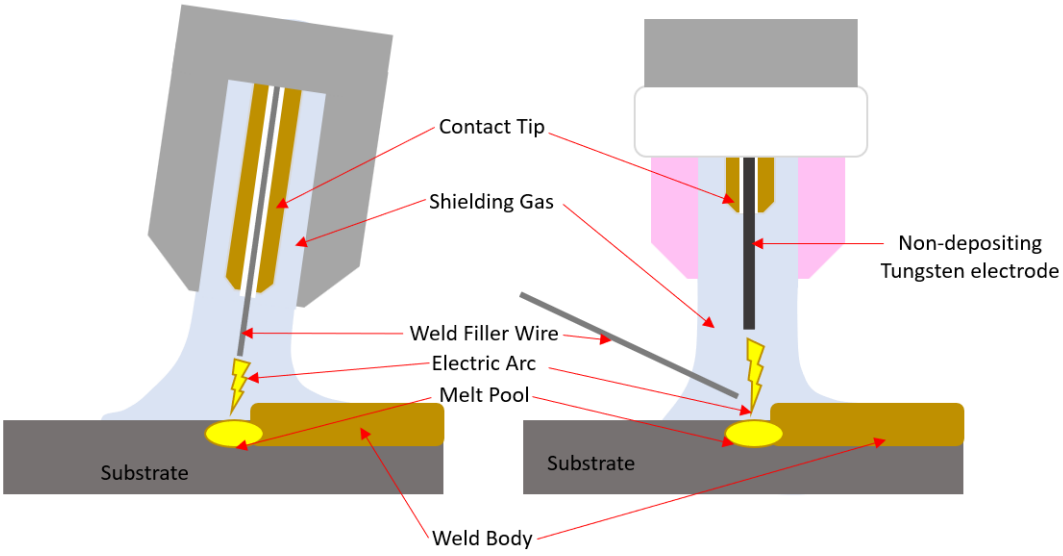

Figure 7: In MIG welding, the arc is formed between the filler wire and substrate (left), while in TIG welding, the arc is formed between a tungsten electrode, and the filler wire is introduced from the side (right).

As the TIG torch is moved, the melt "pool" is dragged along with the torch, with the weld material constantly solidifying in its wake. The size and geometry of this melt pool are influenced by the power output of the welder, the speed at which the torch travels, the amount of filler wire deposited per distance traveled, and the positioning of the TIG torch [9]. The final criterion for a welding power supply is a high-frequency start option. A high-frequency start is a setting that allows a plasma arc to be formed between the tungsten electrode and the substrate over a relatively large distance. At a steady state, TIG welding with steel only requires a DC (direct current) power source; however, DC power alone is not suitable to reliably initiate the arc across the desired distance at the beginning of a welding pass. The high-frequency start provides a high-frequency AC (alternating current) to the welding torch head, which helps initiate the arc, after which the DC power source is applied for the rest of the weld pass. Other starting methods require the electrode to briefly touch the substrate before an arc forms, but this is problematic, as during WAM, weld deposits can vary in height, and the length of the electrode may also change due to degradation. The challenge of varying electrode-to-workpiece distances is avoided with the high-frequency start function. One complexity added by a high-frequency start function is the introduction of strong EMF (electromagnetic field) waves, which can interfere with nearby electronics. A Miller Dynasty 280 (SKU: 907514) is used to fill the role of the welding power supply.

In a more conventional scenario, CNC tables are equipped with a spindle and mill-bit attachment on the tool head, which is utilized for cutting material. For the WAM printer, this tool head is a TIG torch connected to the welding power supply (Figure 8). The work area on the CNC table is a large steel plate electrically insulated from the CNC baseplate with a concrete board. A water-cooled copper chill plate is bolted to the steel plate for supplemental cooling. Substrates for printing are clamped to this build area prior to printing.

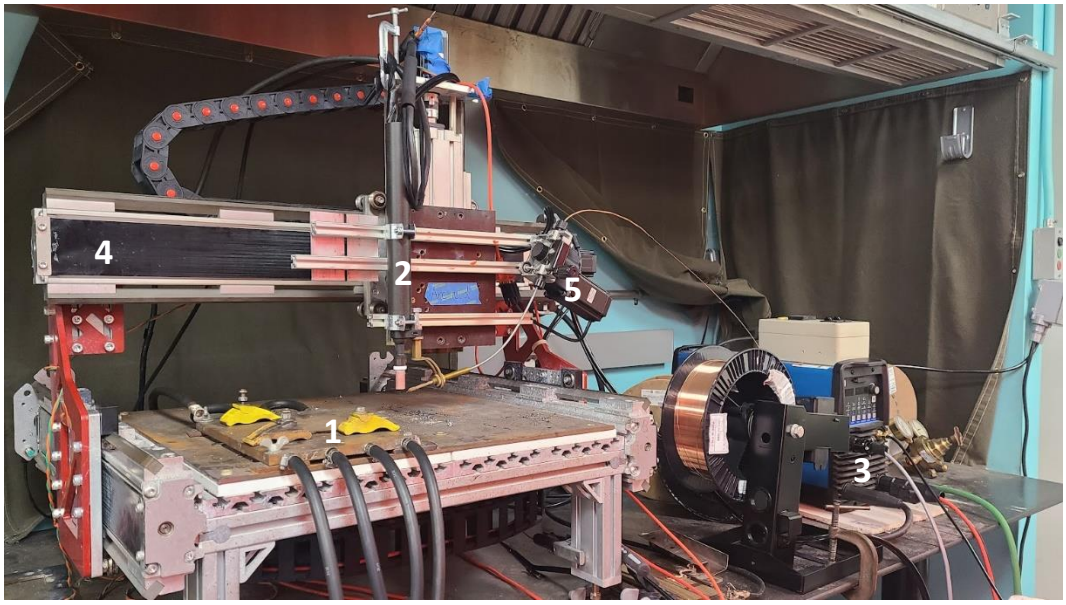

Figure 8: WAM printer set up. 1: copper chill plate, 2: TIG welding torch, 3: Miller dynasty 280 welder, 4: AvidCNC benchtop CNC table, 5: Axis driven wire feed

There is no native connection between the AvidCNC control box and the Miller Dynasty 280 welder. Being able to control the functions of the welder through the CNC control box and, consequently, the print programs were necessary. The main two functions controlled were the torch on-off signal and a variable voltage signal that

adjusts the amperage output during welding. To accomplish this, a custom cable box was built to route signals for controlling a spindle from the control box to proxy the foot switch inputs on the welder. Both of these are 14-pin type connections, albeit with different configurations (Figure 9, Figure 10). The torch on-off function only required the completion of a circuit between two pins on the welder (A and B). This was accomplished by routing the pins through a commercially available optocoupler, which completed the connection between the pins when given a 5-volt input signal. The signal used would have otherwise controlled one of the box's two 120V AC relays. Turning on "Relay 1" in the software activates the torch. A 0 – 10v variable input signal controls the amperage of the welder; this signal was proxied by a matching 0 – 10v variable output signal from the CNC box that would normally control a spindle speed. Both these signals were referenced to a different ground voltage associated with each device; direct wiring might have proved detrimental to the electronics. To keep these signals separate, a commercially available isolation circuit was used to mirror the control box voltage onto the welder input. To prevent interference from EMF waves of the high-frequency start, these wires were run through a shielded cable and box grounded to the frame of the CNC control box.

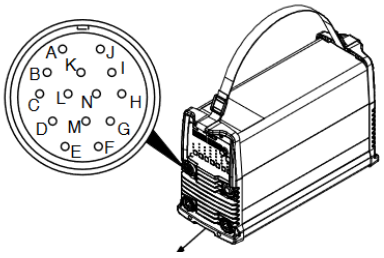

15 VOLTS DC OUTPUT CONTACTOR	A	Contactor control +15 volts DC, referenced to G.
	B	Contact closure to A completes 15 volts DC contactor control circuit and enables output.
REMOTE OUTPUT CONTROL	C	Output to remote control; +10 volts DC output to remote control.
	D	Remote control circuit common.
	E	0 to +10 volts DC input command signal from remote control. *Reconfigurable as input for Output Enable (Weld Stop) – used to remotely stop the weld outside the normal welding cycle. Connection to the D socket must be maintained at all times. If the connection is broken, output stops, and Auto Stop is displayed.

Figure 9: 14-pin input connection on the welder[10]. Pin functions shown are used by the adaptor cable where A and B initiate the ARC, and D and E modulate the amperage.

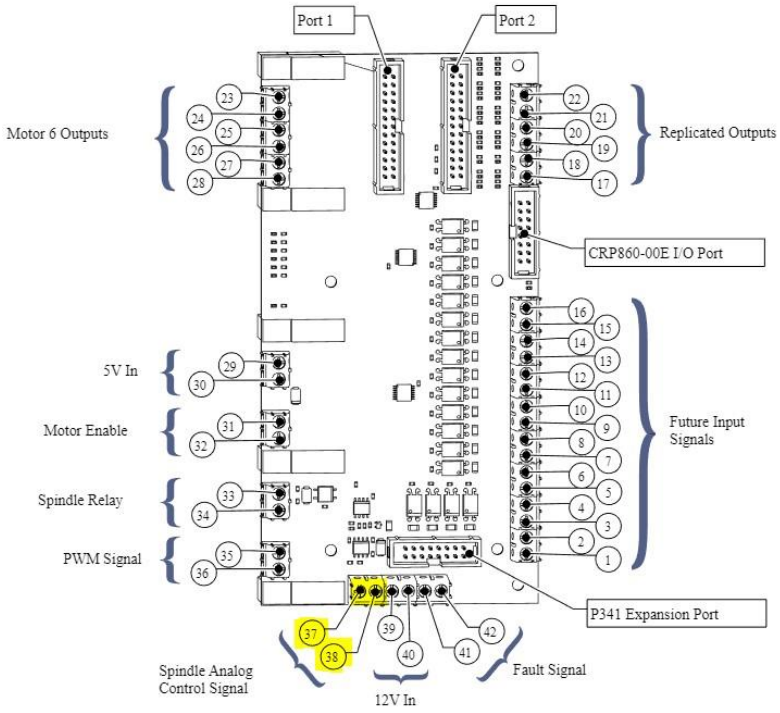

Figure 10: The main circuit board in the CNC control box (Jake G. AvidCNC support, personal communication, September 2, 2022). The variable 0-10v signal is produced between contacts 37 and 38. This signal is routed through an isolation circuit to produce a matching voltage between welder pins D and E. This controls the welding amperage.

As previously mentioned, the movement of the tool head is being controlled by an AvidCNC system utilizing Mach4 software on a nearby desktop. Third-party software is installed on the computer in order to generate tool-paths, which the welding torch will follow to produce the printed part. Tool paths are written in a type of code called “G-code.” There is a large variety of commands in G-code writing that are universally shared across every software program, and there are several specific to the capabilities of Mach-4 and the AvidCNC control box. Standard uses of CNC utilize a designated postprocessor in a CAM (computer-aided manufacturing) software package of choice to create tool-paths from a given geometry. These will take into account the different types of tool heads being used and machine dimensions because this instance of custom WAM printing is vastly different than a milling operation that may be calculated using CAM software. The generation of tool-path G-code files used in printing requires custom programming.

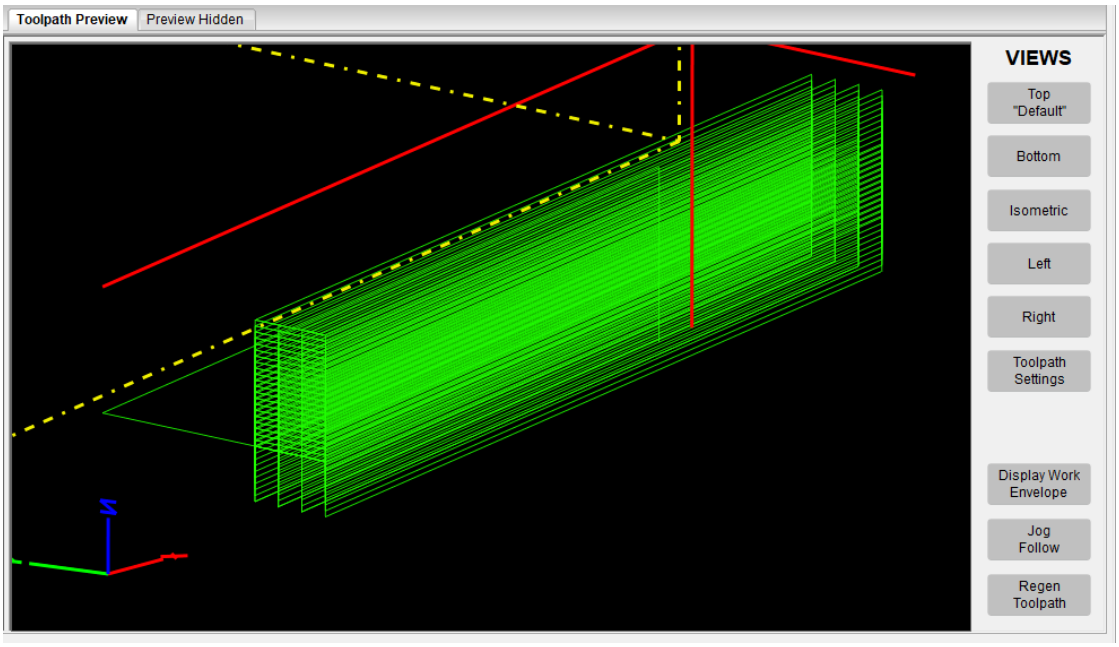

Figure 11: Tool path preview in Mach4 software. The CNC table gantry will make the tool head trace this path (green lines). The particular path shown is a linear raster of a 100mm long, 18-layer high print. The simplicity of the shape allowed for programming in MATLAB.

Had the complexity of the printed samples required, a custom postprocessor could be written in one of these CAM software packages that would provide a printing toolpath for a given geometry. For the simple rectangular deposits that were needed for rotary bend fatigue samples, a custom program was written in MATLAB. This program takes a variety of user inputs relating to the dimensions of the rectangular deposit and the deposition process and returns a G-code. These files can then be loaded into the Mach-4 software, and the WAM printer will commence with printing the resultant shape.

Material Selection

For WAM printing, there are two different material selections that need to take place. The first is for the weld filler wire that will be making the bulk of the deposit. The second selection is that of the substrate to which the first layer of the WAM deposit will be welded. For the final use case of the WAM deposits, the material will be welded into a notch on a grade-E casting. In order to simulate conditions nearest to this, portions of thick cast grade-e were utilized as substrates. These were produced from solid portions of Y-block risers previously cast at Michigan Tech. All WAM deposit rotary bend fatigue specimens were printed on a grade-E substrate. During process development, 3/16" 1018 steel plate was utilized as cheap and available substrate material. Criteria for a suitable filler wire included several factors. It should be similar in ultimate tensile strength to that of the grade-E cast steel. It should not rely on carbon as its main strengthening factor. It should be readily commercially available. Lastly, the inclusion of slight alloying elements could potentially increase its corrosion performance. For this, an "ER120s-1" wire with a 0.035" diameter was selected with "ER110s-1" as a secondary option.

Table 3: Chemical composition of suitable weld filler wire as measured with optical electron spectroscopy (OES)

Material	UTS (KSI)	C	Si	Mn	Ni	Cr	Mo	P	S
ER120s-1	120	0.093	0.39	1.32	1.70	0.22	0.31	0.01	0.01
ER110s-1	110	0.085	0.40	1.51	1.93	0.07	0.27	0.01	0.01
Grade-E Target		0.25	0.42	1.3	N/A	N/A	N/A	<0.02	<0.02

Printing Process

During the development of printed WAM samples, two different tool-path creation strategies were used. Both of these approaches were realized in the form of G-code files, which Mach4 interprets for the printer. The first approach used is the most straightforward; this shall be referred to as a linear raster tool path. The second approach used is a bit more complicated but is commonplace in 3D filament printers; this shall be referred to as a square raster tool-path. While first developing suitable printing parameters, the easiest test print possible consists of a single straight-printed bead. In producing larger structures, the most direct translation is to layer these printed beads, one next to another, then on top of another. Each pass of the welding arc resulted in another straight line being added to the structure; hence linear raster. The width of these structures would be controlled by the number of printed lines next to each other. The square raster approach is slightly different; instead of depositing the entire length of the print and repeating, the tool-path zig-zags across the width of the build for the total length. It ends up producing a similar shape to a square wave; hence square raster. Although WAM deposits display slight amounts of anisotropy, the deposition pattern has little effect on the end properties [11]. This allows for the choice of raster pattern used to mainly focus on increasing the efficiency and consistency of the printing process.

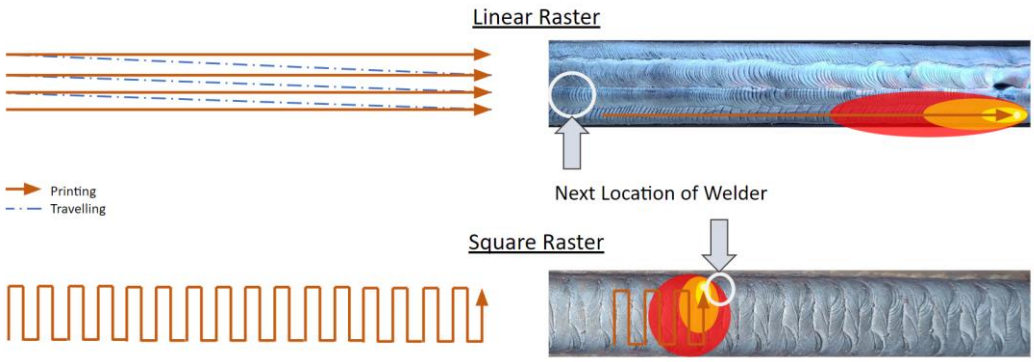

Figure 12: An individual layer traveled in a linear raster pattern, and a layer traveled in a square raster. The square raster allows for better heat efficiency due to the local heat concentration.

A benefit the square raster has over the linear raster is related to the localization of heat in the substrate. Previously deposited WAM material and the printing substrate are in a constant flux of heat being added via the welding arc and heat being removed. Depending on the grade of wire used in the welding application, different amounts of pre-heat of the substrate may be called for. For the commercially available weld wire being used, a pre-heat temperature of 300°F was recommended. During the linear raster path, whenever a new line segment is started, it is after the torch head travels to the location furthest from the area of the most recent heat application. With a square raster, each new line segment is deposited directly next to the area of the most recent heat application. This arrangement helps the substrate remain at a high preheat temperature, enabling easier and more consistent welding (M. Kletchka, personal communication, October 1, 2021).

Table 4: Parameters used for printing WAM samples

Printing Parameter	*Value*
Starting amperage	110 Amps
Amperage decrease per layer	-0.7 Amps
Horizontal bead spacing	2.9 mm
Layer height increase	0.82 mm
Wire extrusion per mm traveled	3.81 mm
"Total" starting travel speed	"F704"
Starting travel speed in the X-Y plane	2.97 mm/s
Speed increase by end of print	30%
Pause between layers	60 s

To ensure print repeatability, operators were trained to monitor the printing process for any issues that may arise in addition to preparing the print area, machine, and printing program. Unless errors arose with the printer itself, intervention was often unnecessary apart from ensuring the first layers had adequate pre-heat. Visual and audio indication was used to ensure weld beads were depositing smoothly and adhering to previously deposited material.

Sample Preparation and Testing

Once a standard set of printing parameters was established, small “half” samples (Figure 13) were produced to confirm the quality of the WAM prints prior to time-consuming, full-scale printing for rotary bend fatigue testing (Figure 14). In addition, baseline samples of the Grade-E material were processed from the Michigan Tech cast y-blocks and keel blocks from Amsted Rail (Figure 15). Although the top of the y-block acts as a riser and may be riddled with porosity, measurements were taken from the reduced section at the bottom typically viewed as sound cast material. Likewise, the keel blocks were procured from the bottom of a much larger casting, where the smaller volume produces the fastest cooling rate in addition to having ample molten material available to prevent shrinkage porosity. Both materials will provide fair comparisons.

Figure 13: A "half" 40 mm long sample with a shorter print time for property testing. The substrate is a 1018 mild steel plate.

Figure 14: WAMA 160 mm long WAM print, which can be machined into two hour-glass rotary bend fatigue samples. Substrate is a Grade-E y-block riser.

Figure 15: Michigan Tech cast Grade-E y-block (left) and a cast Grade-E keel block provided by Amsted Rail (right). The keel blocks were machined into rotary bend fatigue samples to provide baseline data.

All full-size prints for the fatigue samples, baseline Grade-E keel blocks, and select half samples were heat treated in the same way as production Grade-E knuckles. Given the reduced size of the samples compared to the knuckles, less heating time was required for each step. Samples were austenitized in a Thermolyne furnace set at 954°C (1750°F), and then water was quenched at 110°F, with the rising temperature mitigated by adding cooler water (Figure 16). Tempering was done in a standard heat treat oven at 593°C (1100°F).

Figure 16: A WAM printed sample just after austenitization and before being quenched.

Metallographic samples were sectioned from the samples produced during the parameter tuning steps and from the cast baseline materials. They were then ground with increasing grits of metallurgical paper up to 1600 grit, then final polished with 1 μm Dialube. To reveal microconstituents, a 2% Nital solution was used to etch the surface of the polished sample until the surface appeared as a faint grey and was then rinsed off. Micrographs were compared between the as-printed and post heat-treated states. Additionally, grain size was measured on a heat-treated WAM sample, three images were taken at 100x magnification each for the top, middle, and bottom of the

print. Grain boundary intersections were then marked in Olympus Stream Essentials to calculate the size using a method defined in ASTM E 112-13.

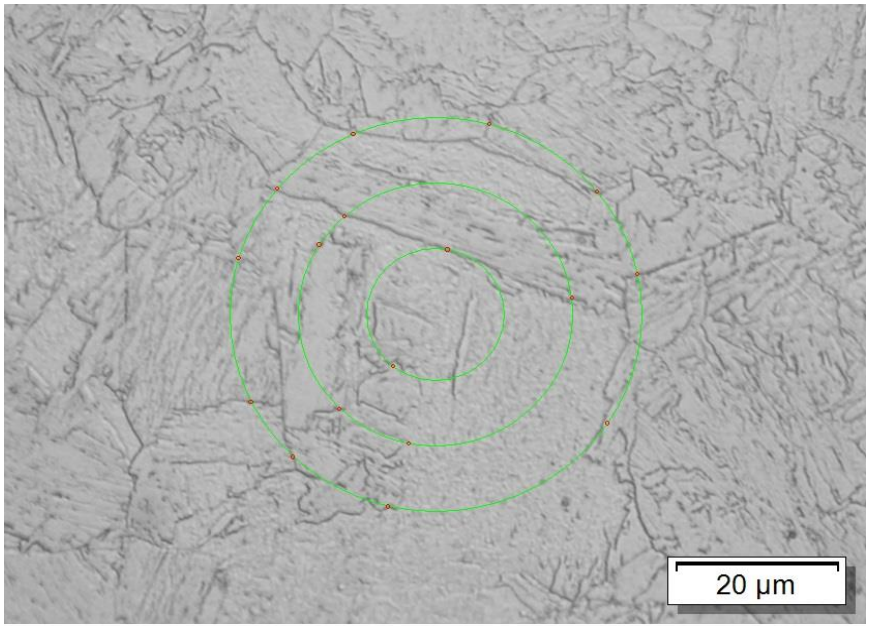

Figure 17: Grain size being measured. Grain boundary intersections (red dots) with the green concentric circles are used in calculating the grain size.

Some of the unetched samples were analyzed for porosity by capturing five images at semi-random locations. These images were quantified with Olympus Stream Essentials (version 2.4.2) software (Figure 18). Porosity appears dark in the microscope, and adjusting the focus causes various depths within the pores to come in and out of view. This technique was used to avoid dark regions that were not porosity. The phase analysis function was used to highlight the high-contrast pores. Porosity metrics measured included pore volume fraction, number, and sphericity, allowing for comparison of defects between the WAM prints and the baseline Grade-E substrates.

Image Number	Phase	Fraction [%]	Image Name	Image Comment
1	1	0.53	YAC_2.jpg	

Image:

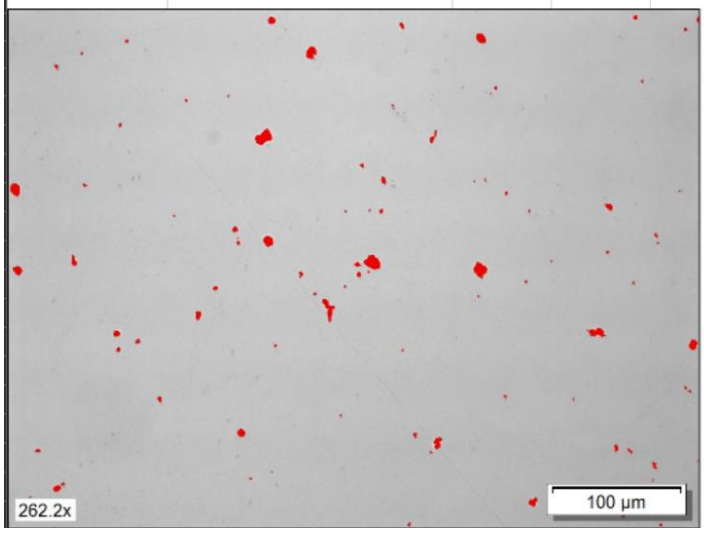

Figure 18: Pores highlighted in red by the Olympus software in a cast y-block sample.

Hardness was assessed on printed samples, y-block samples, and keel block samples before and after heat treatment to compare with the Grade-E specification. Brinell hardness was measured with at least 5 replicates per sample with a 10 mm diameter tungsten carbide ball loaded to 3000 kg for 10 s. The resulting diameter of the indentation was measured with a BOSS camera system to compute the Brinell hardness value.

To track local element concentrations and gradients within the printed structure, both an as-printed sample and a heat-treated sample were assessed with energy dispersive spectroscopy (EDS) in a scanning electron microscope (Philips XL 40 ESEM). Line scans, 2.4 mm long, were measured at 20 keV near the bottom of the print, extending towards the top (Figure 19).

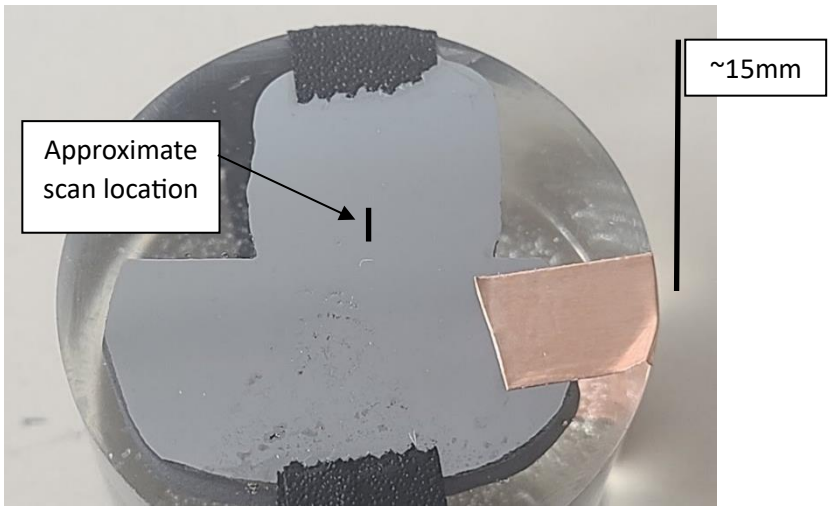

Figure 19: WAM print prepared with conductive tape SEM-EDS analysis, with the approximate location of the 2.4mm scan marked.

In addition to using EDS to attempt to track diffusion, an estimation of the diffusion distance of carbon into the austenite of the WAM print during heat-treatment was calculated (Equation 1).

$$x \approx \sqrt{Dt}$$

$$D = 16.2 * 10^{-6} exp(\frac{-137800}{R * T})$$

Equation 1: Estimation of diffusion length, x is the length in meters, t is the time in seconds at temperature, D is the diffusion coefficient of carbon in austenite between 800°C and 1000°C [12], R is the universal gas constant, and T is the heat treat temperature in kelvin.

After heat treatment, the large WAM prints and keel blocks were machined into a rotary bend fatigue specimen shape (Figure 20). Each WAM deposit accommodated two samples end to end. Once machined, the tapered center section was hand-polished to 600 grit to remove any machining lines. A smooth surface is required for accurate

fatigue testing, as grooves would produce unwanted stress concentrations, reducing fatigue life.

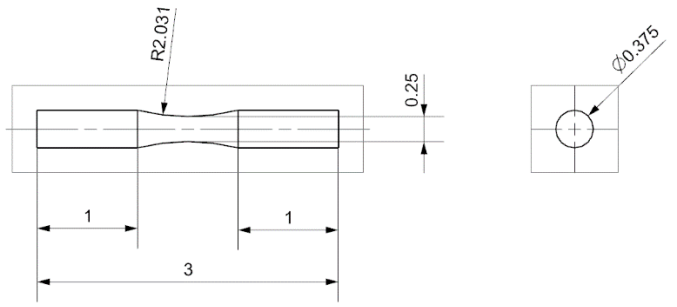

Figure 20: Geometry of "hour-glass" rotary bend fatigue test specimen (inches) where both sides are inserted into collets, and the center is polished to 600 grit.

Two rotary bend test machines were utilized for testing (Figure 21). The diameter of the hourglass section was specified as 0.25," but each sample varied slightly, so the true diameter was measured before testing. This would be used in conjunction with the moment applied to calculate the maximum surface stress (Equation 2). A moment was applied to the samples by an adjustable load arm in increments of 5-inch pounds. Cycles were counted during the test, and the real-time data were used to select the magnitude of the next applied load.

$$Stress = \frac{Moment\ setting\ (in - lbs)}{0.0982 * Reduced\ Diameter\ (in)^3}$$

Equation 2: Calculation of maximum surface stress (psi) for RBF testing.

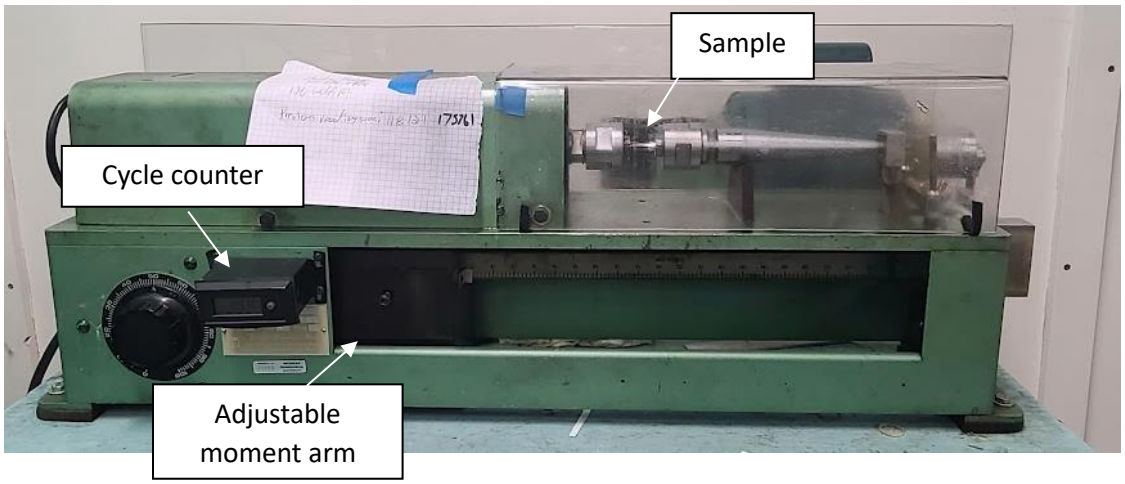

Figure 21: A rotary bend fatigue testing machine.

After the fatigue data was collected, two separate fits were calculated for each test material. One fit predicts the endurance limit, which provides stresses below which the material should never break, and the other predicts the fatigue limit for higher stresses and lower cycles. The low-cycle fatigue curve uses the standard [13] equation:

$$Log(N) = m * Log(S) + c$$

$$Log(S) = \frac{1}{m} Log(N) - \frac{c}{m}$$

Equation 3: The standard fatigue curve equation where N is the number of cycles, S is the stress, m & c are the fitting parameters.

Performing a linear fit on the base 10 log of the data determines the coefficients. Although stress is the independent variable, it is often plotted on the Y-axis; the equation has been rearranged to accommodate this. Predicting the endurance limit followed this equation [13]:

$$Endurance\ limit = S_0 + S_i\left(\frac{A}{F} \pm \frac{1}{2}\right)$$

$$A = \sum_{i=1}^{n} i * f$$

Equation 4: Endurance limit where S_0 is an initial stress, S_i is the difference between equally spaced load levels, i is an integer designation based on the load levels distance from the initial amplitude, F is the total number of runouts, and f is the number of less frequent event at the load level i.

The initial stress (S_0) used for each was the stress at the highest runout. Load level designations (i) decreased from there. Because of the variance in diameter size, S_i was calculated from an average of the stress differences between run-outs.

Results

Micrographs

The following micrographs are of two WAM builds. The first build is as-printed (Figure 22, Figure 23) and exhibits a vastly different microstructure between different areas of the structure. The second build has undergone heat treatment (Figure 24, Figure 25) and exhibits a very similar microstructure from just above the substrate interface to the top of the build.

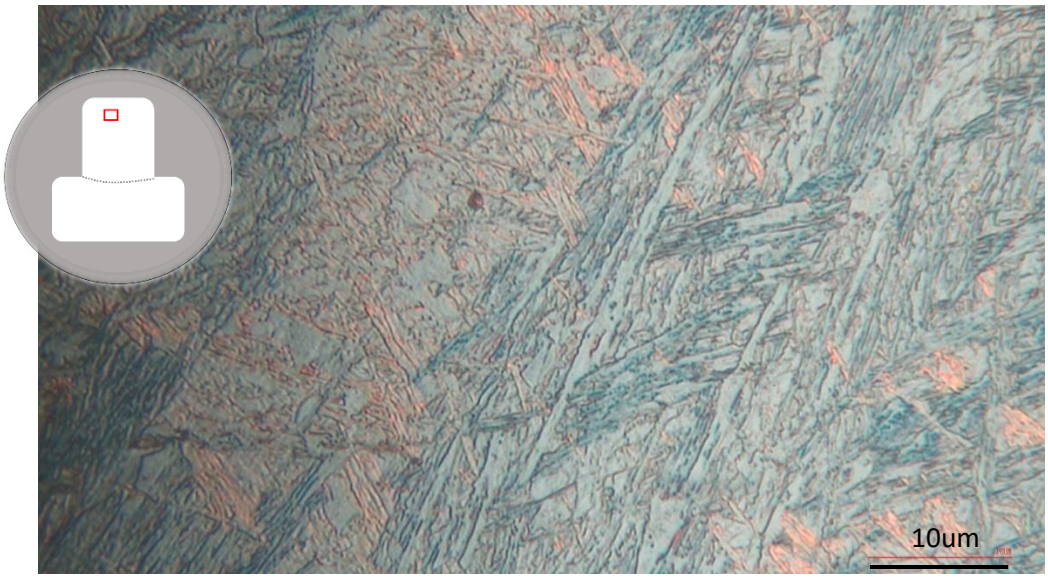

Figure 22. As-printed WAM deposit near the top of the build.

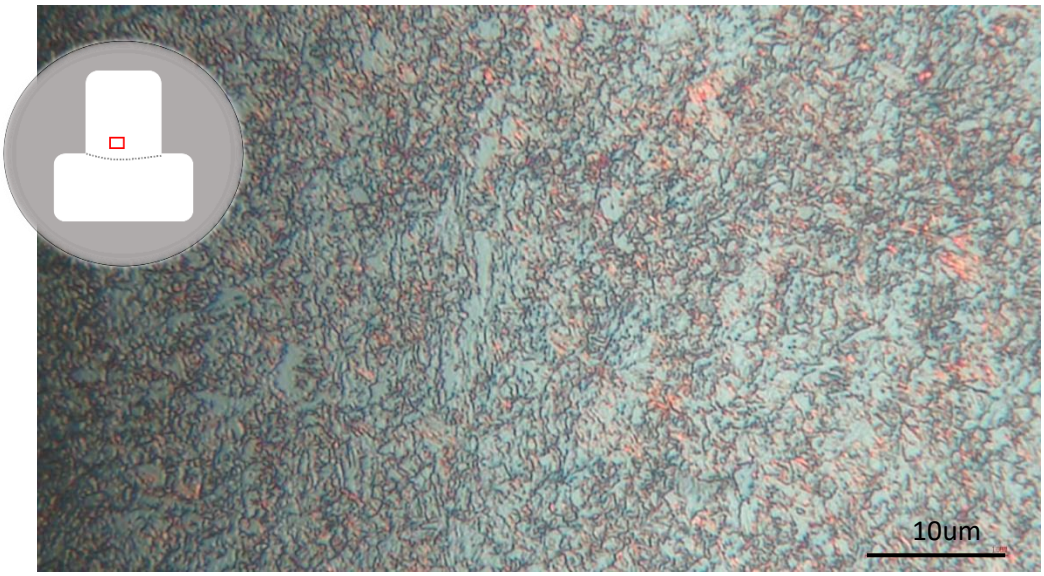

Figure 23: As-printed WAMWAM deposit near the bottom of the build.

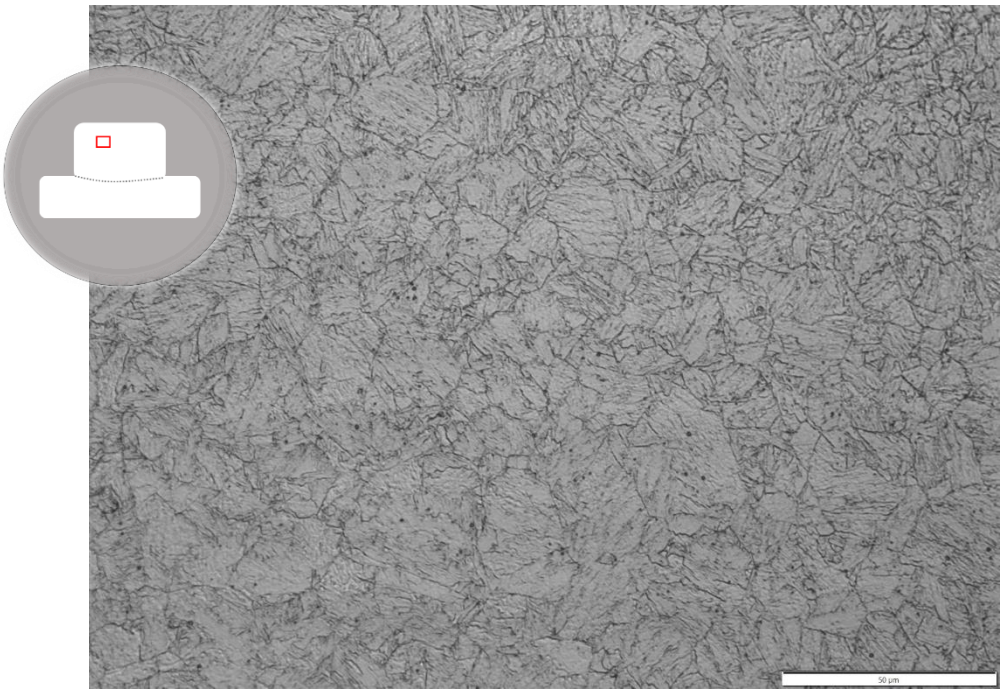

Figure 24: Heat-treated WAM deposit near the top of the build.

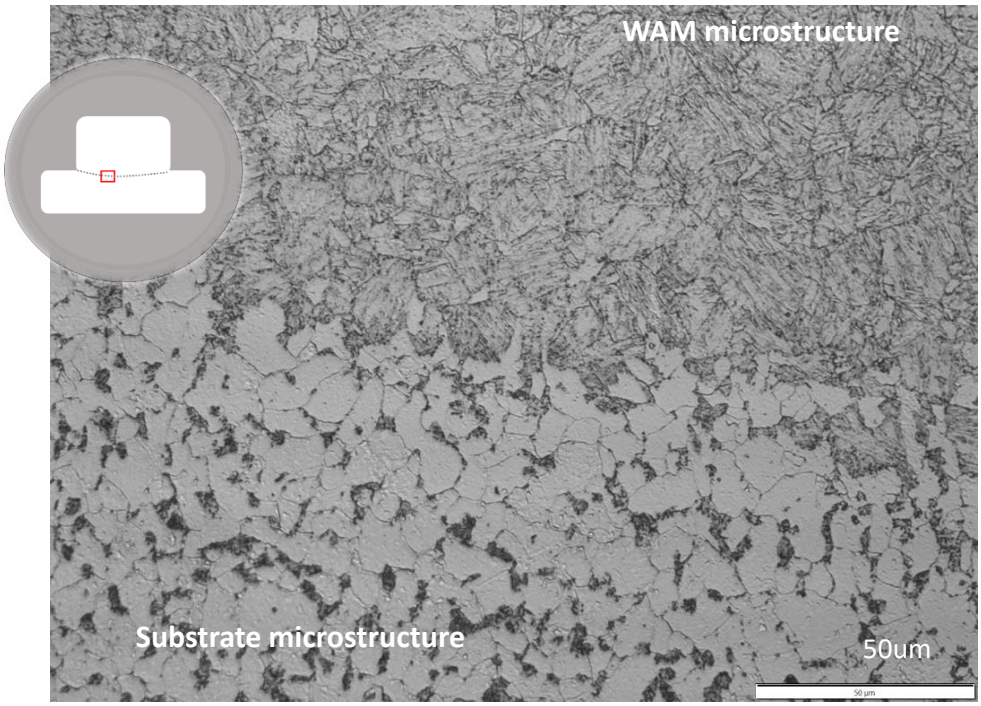

Figure 25: Heat-treated WAM deposit at the interface between the build and the 1018 steel substrate.

Table 5: Mean grain sizes taken throughout the height of the print.

Location	*Mean grain size, G*	*Standard Deviation*
Top of print	8.7	0.6
Middle of print	8.8	0.3
Bottom of print	8.4	0.2

Defects

The data from the Olympus image analysis was imported into Minitab for a one-way ANOVA analysis of multiple means using the Tukey method. Data sets that share the same grouping letter designation (A or B) are statistically equivalent (Figure 26, Figure 27).

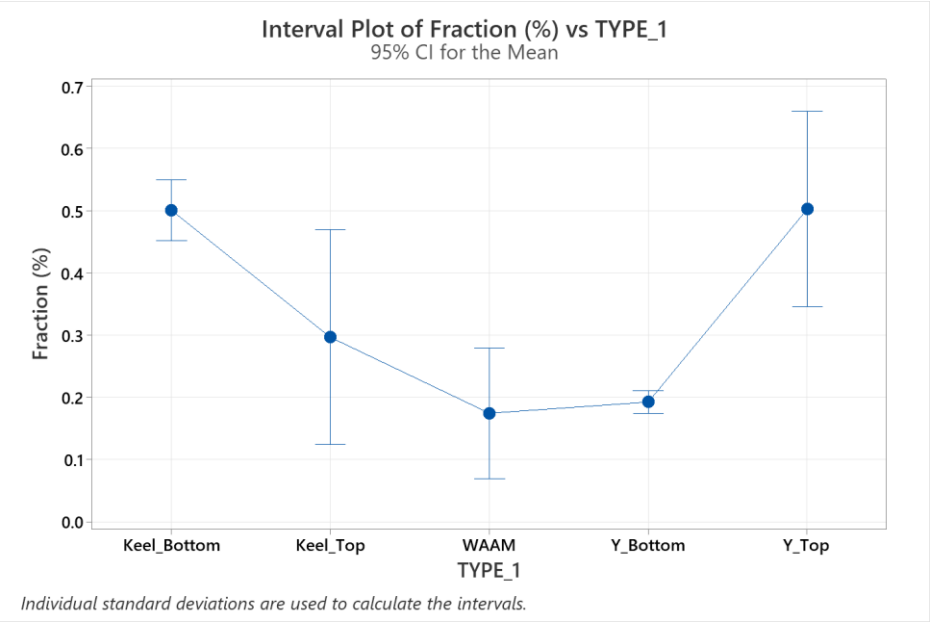

Grouping Information Using the Tukey Method and 95% Confidence

TYPE_1	N	Mean	Grouping
Y_Top	5	0.502	A
Keel_Bottom	5	0.500	A
Keel_Top	5	0.296	B
Y_Bottom	5	0.192	B
WAAM	5	0.174	B

Means that do not share a letter are significantly different.

Figure 26: One-way ANOVA with Tukey method for porosity volume fraction.

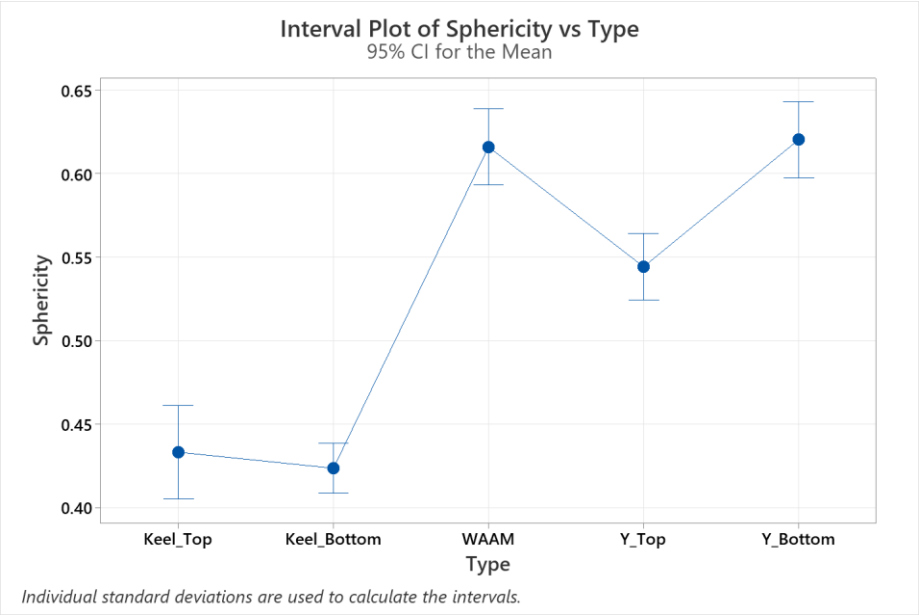

Grouping Information Using the Tukey Method and 95% Confidence

Type	N	Mean	Grouping		
Y_Bottom	390	0.620231	A		
WAAM	368	0.615924	A		
Y_Top	587	0.544106		B	
Keel_Top	280	0.433036			C
Keel_Bottom	1019	0.423435			C

Means that do not share a letter are significantly different

Figure 27: One-way ANOVA with Tukey method for pore sphericity

Hardness

The Brinell hardness measurements were analyzed in Minitab to compare the WAM sections to the Grade-E y-block and Grade-E keel block in both the as-produced and heat-treated state (Figure 28).

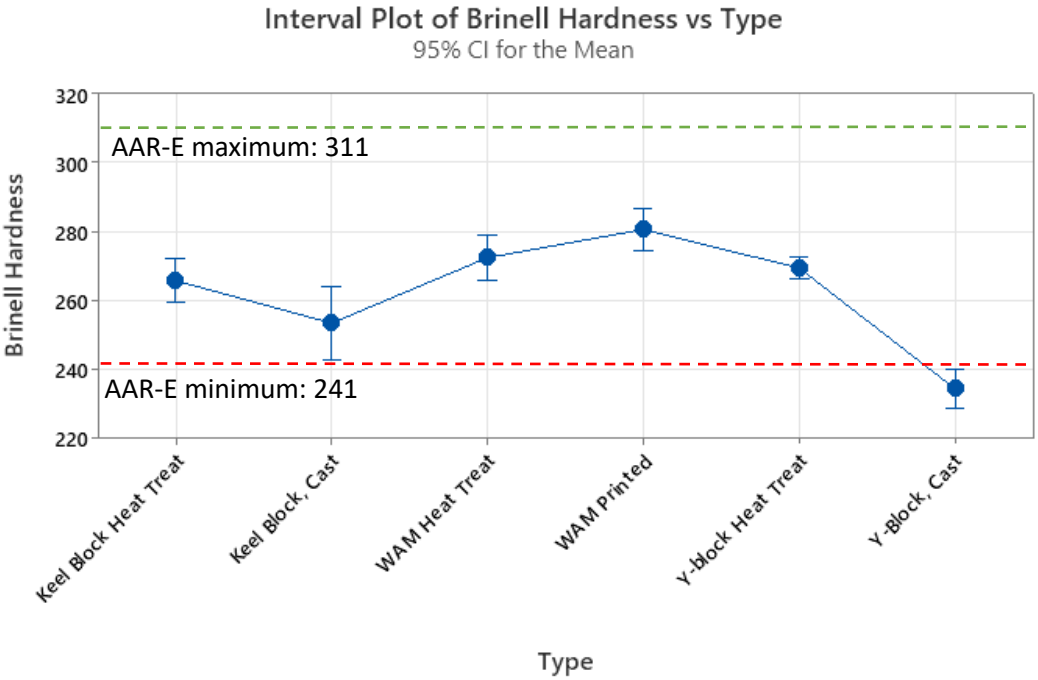

Grouping Information Using the Tukey Method and 95% Confidence

Type	N	Mean	Grouping
WAM Printed	6	280.667	A
WAM Heat Treat	6	272.500	A B
Y-block Heat Treat	6	269.500	A B
Keel Block Heat Treat	6	265.833	B
Keel Block, Cast	6	253.500	C
Y-Block, Cast	6	234.500	D

Means that do not share a letter are significantly different.

Figure 28: One-way ANOVA and Tukey method for Brinell hardness.

SEM

The line scans done with the EDS were subdivided into 10 equally spaced points. At each point, a composition reading was taken, allowing for the composition to be plotted as a function of distance. Shown here (Figure 29, Figure 30) are the plotted compositions near the base of the WAM build in both an as-printed and heat-treated state. Carbon is not reliably measured with EDS; however, the rough estimate predicts a diffusion distance of 0.4 mm from holding at 1750°F for 2 hours.

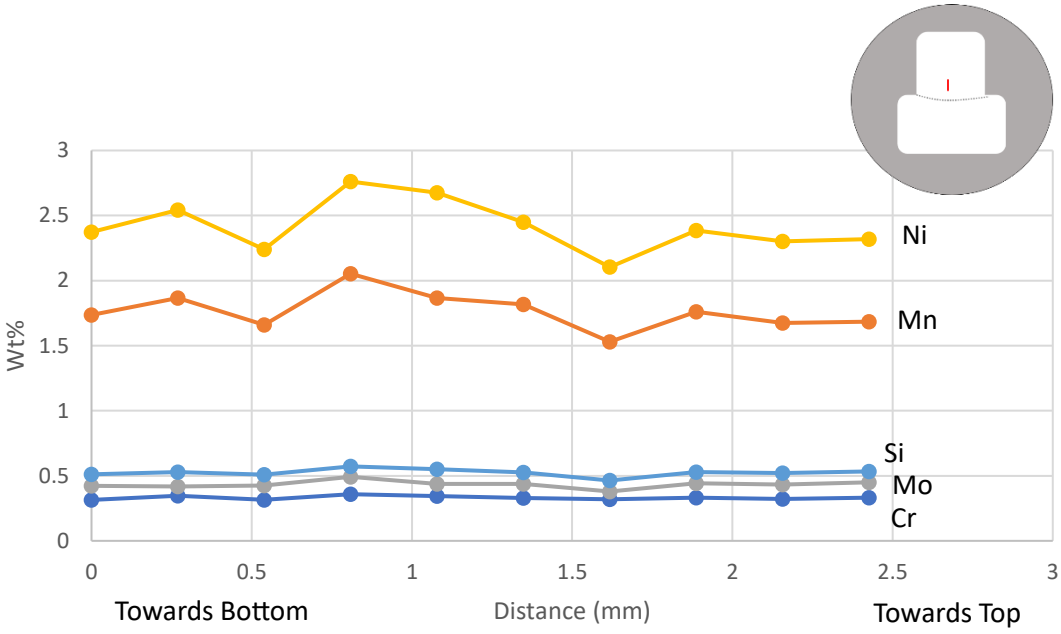

Figure 29: EDS line scan of WAM sample as-printed.

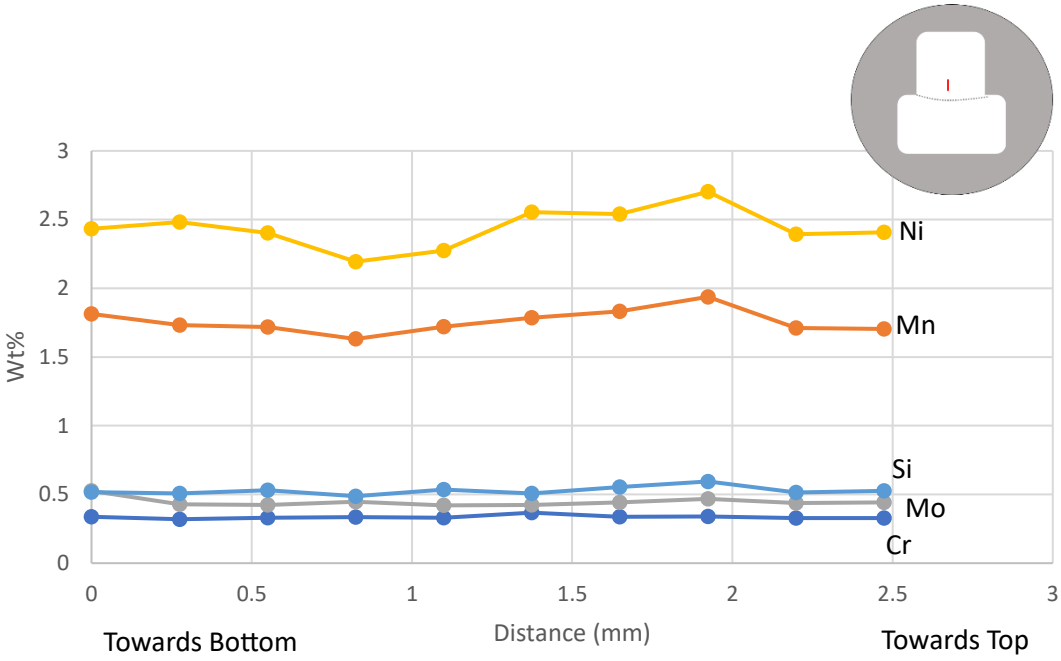

Figure 30: EDS line scan of WAM sample after heat treatment.

Rotary Bend Fatigue

RBF samples are tested at various loading conditions; when the sample breaks, the number of cycles it survives is recorded. The stress from the load and the number of cycles it survived are plotted on a semi-log graph to make an "S-N" curve that can be used to predict future failure at load. The plotted data can be fit into a function to provide quantifiable results (Figure 32, Table 6).

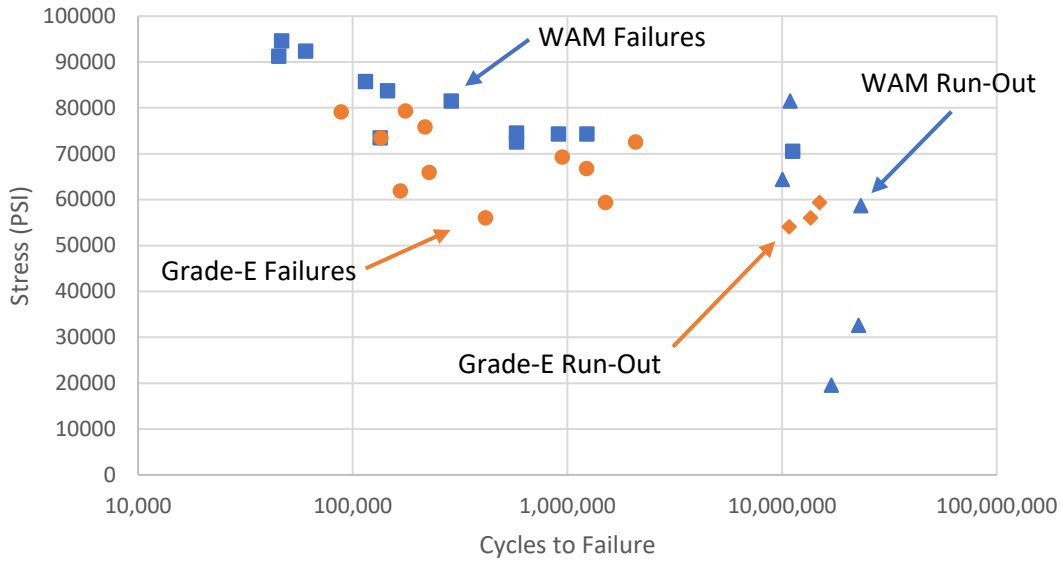

Figure 31: Raw rotary bend fatigue results from WAM and Grade-E samples with cycles to failure on a log scale. Runout is noted when the sample reaches 10,000,000 cycles without breaking.

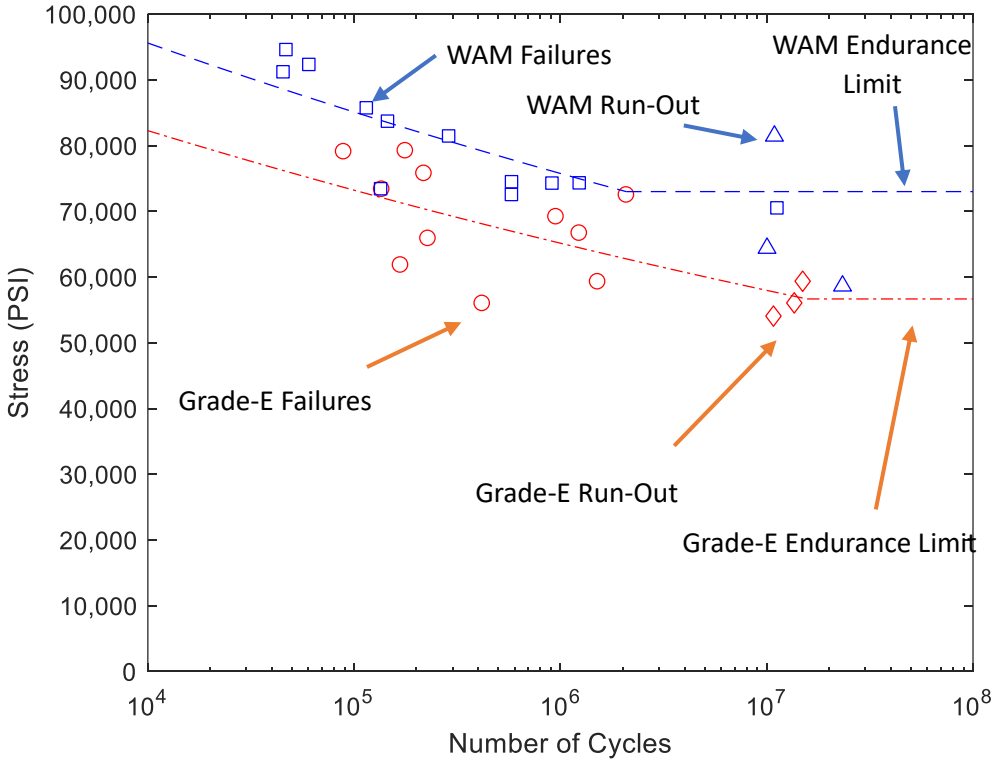

Figure 32: Fatigue test results with predicted fatigue limits

Table 6: Fatigue curve endurance limit and error bounds with calculated constants

	WAM	*Grade-E*
Predicted Endurance Limit	73,000 Psi	56,666 Psi
Endurance Limit error bounds	±2,500 Psi	±2,500 Psi
1/m (as calculated from fit)	-0.0505	-0.0507
-c/m (as calculated from fit)	5.1826	5.1179
m	-19.80	-19.72
c	102.6	100.9

Discussion

The testing performed prior to beginning fatigue testing produced more confidence in the material prior to the time-intensive machining and testing of rotary bend fatigue samples. Each test in isolation is not enough to prove the WAM material will perform better, but when coupled with the fatigue results, it is able to produce a clearer picture.

Due to the process of WAM printing, the thermal history and microstructure between the top and bottom of a print can vary significantly [14]. While the top layer of a print may have only been solidified once, deeper layers have gone through several cycles of melting and/or heating and cooling. This difference produces a vastly different microstructure from top to bottom (Figure 22, Figure 23), and had the rotary bend fatigue samples not been heat treated, more variations would likely have been

observed in the fatigue results due to the inhomogeneity of the microstructure. After the Grade-E steel heat treatment schedule, the microstructure appears much more uniform (Figure 24, Figure 25). Qualitatively, a visually similar microstructure can be observed throughout the entire height of the deposit. Grain size number averages falling between 8 and 9 also indicate the homogeneity of the WAM print after heat-treatment. The similarities are especially noticeable when compared with that of the non-heat-treated sample (Figure 22, Figure 23).

The second validation takes into account the defects in the material, as defects such as porosity can reduce the strength, ductility, and fatigue life. The presence of defects in the material acts as initiation points for cracks to nucleate and then grow, leading to premature failure in both normal loading and cyclic loading. A common defect in both a WAM build and casting is microporosity. Limiting the size and fraction of microporosity reduces the chance of cracks forming that cause premature failure. Additionally, the shape of the micropores can impact crack formation, with spherical pores being less likely to initiate cracks than jagged ones. Sphericity can be quantified on a scale of 0 to 1, with 1 being the most spherical (Figure 33). A sharp corner of a jagged pore induces a local high-stress concentration, which further increases the likelihood of cracking.

Figure 33: Exaggerated representation of sphericity. Jagged edges on less spherical pores are more likely to initiate cracks.

From a Tukey analysis of the porosity fraction (Figure 26), the WAM displays the lowest mean porosity but is statistically similar to samples taken from the top of a cast keel block and the bottom of a cast y-block while having less porosity than two other sample locations in the cast specimens. This suggests that the WAM deposits have similar or fewer defect fractions as the base cast material, implying that the printing process does not introduce more porosity that can lower the strength and fatigue life. A Tukey analysis of the sphericity of the pores in the different materials provides a similar result (Figure 27). The WAM pores have a similar level of sphericity as the samples taken from the bottom of the y-block, which are more spherical than the cast steel locations. The printing process produces an equivalent, if not superior, material in terms of the shape of the porosity. If the WAM had a higher number of less spherical defects, fatigue failure would likely be sooner and more erratically. The relatively large variation of data points in the Grade-E material suggests that the variety of volume fraction and shape of defects could lead to premature failure.

Hardness is often used as an indicator of tensile strength [15], and for the cast knuckle, it is desired that the WAM deposit does not have a lower or higher tensile strength so it still acts as an overload fuse and breaks in overload conditions, while still carrying the design loads. Meeting the Grade-E hardness specifications ensures WAM's compatibility production. After the Grade-E heat treatment schedule, all three sample types were within the hardness specification for the AAR E standard and are statistically similar to each other (Figure 28). This indicates that the tensile strength of the heat-treated WAM deposits is not significantly different than that of the Grade-E baseline. While a stronger material would also exhibit an increased fatigue life, this would not be desired in a railcar knuckle, as any perceived fatigue life increases should be due to the improved microstructure of the weld filler.

Line scans from the SEM were initially performed to quantify carbon diffusion from the Grade-E substrate into the WAM deposit. A diffusion gradient might have been visible, but carbon is unreliably detected by EDS. The calculated diffusion length of 0.4 mm was sufficient to suggest that any portions of the WAM build with extra carbon content would be removed during machining. Had carbon diffused extensively through the WAM build during heat treatment, RBF samples would have a undesired properties gradient. Heavier, metallic elements are better able to be quantified by EDS, but no discernable gradients were evident (Figure 29, Figure 30). However, fluctuations were present in the nickel and manganese concentrations, with the spacing corresponding to the height of the individual weld beads in the stack. White striations become visible on as-printed WAM builds after etching that also roughly match the

bead height spacing (*Figure 34*, *Figure 35*). These local variations in Ni and Mn are due to segregation during the solidification of the weld bead *[6]*. These fluctuations are still present in the line scans after heat treatment, indicating this cycle is not fully mitigating this segregation.

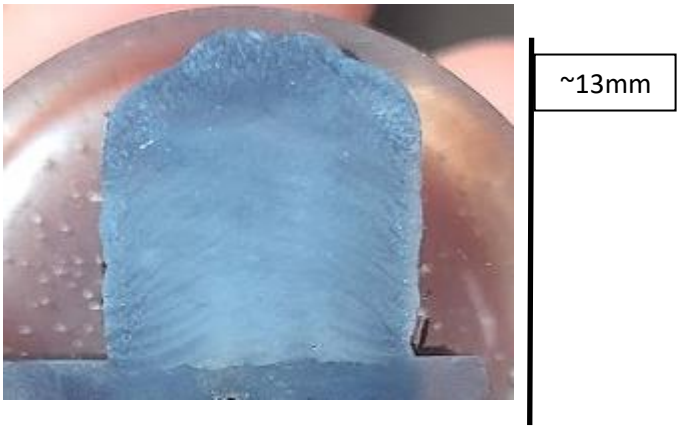

Figure 34: Polished and etched as-printed WAM sample used in the line scan. White striations mimic the profiles of the individual weld beads deposited to print the sample.

Figure 35: Highly visible weld bead profiles on a WAM build after an hour-long submersion in a dilute HCl solution

The RBF results (Figure 32) indicate that the WAM print exhibits superior fatigue performance compared to the Grade-E casting. It has a greater predicted endurance limit (Table 6) and a higher fatigue limit during high-stress loading cycles.

Stresses that are less than the endurance limit are thought to never lead to fatigue failure, regardless of the number of cycles. This endurance limit is visible in the graph as the horizontal line going right to higher cycles. Higher endurance limits allow for a wider range of loads to safely be applied to the material. For example, the railcar might experience a condition that produces a 65 ksi stress in the pulling lug of the knuckle, but this will not break the material instantly because it is below the tensile strength of 120 ksi. However, after one million cycles, the Grade-E will fail at this load, but if this high-stress region of the pulling lug was replaced with the WAM deposit, a 65 ksi stress would never cause failure because it is below the endurance limit. Similarly, where a 75 ksi stress may cause the Grade-E casting to fail around 100,000 cycles, a WAM deposit may be able to last one million cycles.

Conclusions

A more fatigue-resistant substitute for plain carbon cast steel couplers used in the rail industry was able to be produced utilizing a well-controlled TIG WAM process with commercial steel filler wire. The WAM material made from “ER120s-1” filler wire was able to outperform the rail industry’s Grade-E cast steel in rotary bend fatigue testing utilizing the same quench and temper heat treatment schedule used for Grade-E cast steel. This will allow the local application of a consistent WAM material in high-stress regions of railcar couplers to prevent common failures due to fatigue cracking through minimization of porosity and surface decarburization.

Future Work

Superior fatigue performance in a dry, ideal state is necessary for the WAM material, anything less would have worsened the knuckle's performance. Although the fatigue curve provides hope for the WAM material's performance in various other conditions, there are still tests that need to be run to ensure the viability of material substitution in the knuckle.

The first condition that the WAM material should be tested in is a rotary bend fatigue test, in a salt fog environment. The Grade-E fatigue test will also need to be replicated in this more corrosive environment. A salt solution fog in the air will help facilitate corrosion of the specimen while it is being tested. Surface corrosion on the samples will lead to a weakened surface and promote earlier fatigue cracking. If the WAM material is more corrosion resistant it will likely have higher cycles to failure. There are several considerations that need to be taken into account for a salt fog RBF test. The first is a containment strategy for the corrosive environment. A sealed chamber will need to be constructed that allows pass through of the rotating sample. It will need to contain the fog to keep the environment consistent, and prevent corrosion of the testing equipment. Second is the nature of the corrosive environment, this involves determining the ideal salt solution concentration and potentially a on/off cycle for the fog. An ultrasonic humidifier module may be an efficient way to turn the salt solution into a mist. Lastly, the interaction of the two materials in an environment should be considered. The corrosion properties of the WAM and Grade-E while

coupled together will differ from their properties while separate. Because the two materials will be coupled while in use on a knuckle, coupling them during a corrosive RBF test may better represent reality. This aspect may be easier to study in the next testing condition, flexural fatigue.

RBF testing is an adequate way of testing the WAM and Grade-E materials individually; however, because the WAM material will be welded into the Grade-E knuckle, it is important to see how this condition will react to fatigue stresses. Flexural fatigue testing accomplishes a similar goal to RBF, the uniqueness of the sample geometry and procedure allows the maximum stress to occur across the entire length of a wedge-shaped section. A section of the stressed area should be removed and filled with the WAM deposit; the whole sample would then be heat-treated. This arrangement will allow the WAM deposit, the Grade-E plate, and the heat affected zone of the Grade-E near the weld to be put under the same cyclic stress all at once. With this sample, superior fatigue performance will not be able to be determined from comparing fatigue curves, instead it will be determined from the location at which the sample cracks. If the samples crack solely in the Grade-E portions some distance away from the WAM, then the deposits will likely not negatively affect the material while having better fatigue performance. Doing this test in a corrosive environment should also allow for the interaction effects of the WAM and Grade-E while coupled to be observed.

Other tests could be run to better understand these WAM prints. EDS mapping of an area could better show the Ni and Mn segregation in both as printed and heat-treated samples. X-ray diffraction could also be performed to determine the amount of retained austenite in the as printed condition, and if any is left after heat-treatment.

Bibliography

[1] D. Schwen, *Train coupling AAR*.

[2] R. Boelen, P. Curcio, A. Cowin, and R. Donnelly, "Ore-car coupler performance at BHP-Billiton Iron Ore," *Eng. Fail. Anal.*, vol. 11, no. 2, pp. 221–234, Apr. 2004, doi: 10.1016/j.engfailanal.2003.05.009.

[3] S. P. Chunduru, M. J. Kim, and C. Mirman, "Failure analysis of railroad couplers of AAR type E," *Eng. Fail. Anal.*, vol. 18, no. 1, pp. 374–385, 2011, doi: 10.1016/j.engfailanal.2010.09.016.

[4] Sharma & Associates, Inc., "Enhancing the Safety of Coupler Knuckles." U.S. Department of Transportation Federal Railroad Administration Office of Railroad Policy and Development Office of Research, Development, and Technology Washington, DC 20590, Dec. 2017. [Online]. Available: https://railroads.dot.gov/sites/fra.dot.gov/files/2023-09/Coupler%20Knuckles.pdf

[5] M. Mičian, J. Winczek, R. Koňár, I. Hlavatý, and M. Gucwa, "The Repair of Foundry Defects in Steel Castings Using Welding Technology," *Arch. Foundry Eng.*, 2023, doi: 10.24425/122524.

[6] C. Han *et al.*, "Effect of Solidification Segregation on Microstructure and Mechanical Properties of a Ni-Cr-Mo-V Steel Weld Metal," *Metall. Mater. Trans. Phys. Metall. Mater. Sci.*, vol. 53, no. 4, pp. 1394–1406, 2022, doi: 10.1007/s11661-022-06600-w.

[7] I. de Diego-Calderón *et al.*, "Effect of microstructure on fatigue behavior of advanced high strength steels produced by quenching and partitioning and the role of retained austenite," *Mater. Sci. Eng. Struct. Mater. Prop. Microstruct. Process.*, vol. 641, pp. 215–224, 2015, doi: 10.1016/j.msea.2015.06.034.

[8] T. Smismans, N. Chernovol, B. Lauwers, P. Van Rymenant, and R. Talemi, "Influence of post-heat treatments on fatigue response of low-alloyed carbon-manganese steel material manufactured by Direct Energy Deposition-Arc technique," *Mater. Lett.*, vol. 302, pp. 130465-, 2021, doi: 10.1016/j.matlet.2021.130465.

[9] M. Dinovitzer, X. Chen, J. Laliberte, X. Huang, and H. Frei, "Effect of wire and arc additive manufacturing (WAAM) process parameters on bead geometry and microstructure," *Addit. Manuf.*, vol. 26, pp. 138–146, Mar. 2019, doi: 10.1016/j.addma.2018.12.013.

[10] Miller Electric Mfg. Co., "Miller Dynasty Owner's Manual," May 2017.

[11] C. Huang, P. Kyvelou, R. Zhang, T. Ben Britton, and L. Gardner, "Mechanical testing and microstructural analysis of wire arc additively manufactured steels," *Mater. Des.*, vol. 216, pp. 110544-, 2022, doi: 10.1016/j.matdes.2022.110544.

[12] D. C. Parris and R. B. McLellan, “The diffusivity of carbon in austenite,” *Acta Metall.*, vol. 24, no. 6, pp. 523–528, Jun. 1976, doi: 10.1016/0001-6160(76)90096-1.
[13] P. Strzelecki and J. Sempruch, “Experimental Method for Plotting S-N Curve with a Small Number of Specimens,” *Pol. Marit. Res.*, vol. 23, no. 4, pp. 129–137, 2016, doi: 10.1515/pomr-2016-0079.
[14] Q. Fang *et al.*, “800 MPa Class HSLA Steel Block Part Fabricated by WAAM for Building Applications: Tensile Properties at Ambient and Elevated (600°C) Temperature,” *Adv. Mater. Sci. Eng.*, vol. 2022, pp. 1–13, 2022, doi: 10.1155/2022/3014060.
[15] E. J. Pavlina and C. J. Van Tyne, “Correlation of Yield Strength and Tensile Strength with Hardness for Steels,” *J. Mater. Eng. Perform.*, vol. 17, no. 6, pp. 888–893, 2008, doi: 10.1007/s11665-008-9225-5.